Statistics of surface divergence and their relation to air-water gas transfer velocity

William E. Asher,[1] Hanzhuang Liang,[1] Christopher J. Zappa,[2] Mark R. Loewen,[3] Moniz A. Mukto,[3] Trina M. Litchendorf,[1] and Andrew T. Jessup[1]

Received 15 June 2011; revised 27 March 2012; accepted 2 April 2012; published 24 May 2012.

[1] Air-sea gas fluxes are generally defined in terms of the air/water concentration difference of the gas and the gas transfer velocity, k_L. Because it is difficult to measure k_L in the ocean, it is often parameterized using more easily measured physical properties. Surface divergence theory suggests that infrared (IR) images of the water surface, which contain information concerning the movement of water very near the air-water interface, might be used to estimate k_L. Therefore, a series of experiments testing whether IR imagery could provide a convenient means for estimating the surface divergence applicable to air-sea exchange were conducted in a synthetic jet array tank embedded in a wind tunnel. Gas transfer velocities were measured as a function of wind stress and mechanically generated turbulence; laser-induced fluorescence was used to measure the concentration of carbon dioxide in the top 300 μm of the water surface; IR imagery was used to measure the spatial and temporal distribution of the aqueous skin temperature; and particle image velocimetry was used to measure turbulence at a depth of 1 cm below the air-water interface. It is shown that an estimate of the surface divergence for both wind-shear driven turbulence and mechanically generated turbulence can be derived from the surface skin temperature. The estimates derived from the IR images are compared to velocity field divergences measured by the PIV and to independent estimates of the divergence made using the laser-induced fluorescence data. Divergence is shown to scale with k_L values measured using gaseous tracers as predicted by conceptual models for both wind-driven and mechanically generated turbulence.

Citation: Asher, W. E., H. Liang, C. J. Zappa, M. R. Loewen, M. A. Mukto, T. M. Litchendorf, and A. T. Jessup (2012), Statistics of surface divergence and their relation to air-water gas transfer velocity, *J. Geophys. Res.*, *117*, C05035, doi:10.1029/2011JC007390.

1. Introduction

[2] Measuring air-sea gas fluxes to determine the related gas transfer velocities under all conditions is challenging. For example, the difficulties associated with ship-based operations at high wind speeds can restrict data collection. Ocean chemistry and dynamics can also affect gas transfer measurements. Measurements using the direct covariance method (DCM) are limited to locations where the gas of interest has a large concentration difference between the air and water. The purposeful dual-tracer method (PDTM) is most accurate in regions with a well-defined surface mixed layer or shallow, flat bottom topography. Because of these restrictions, the ability to estimate the transfer velocity using parameterizations defined in terms of more easily measured physical properties would be advantageous. However, the transfer velocity is a function of the near-surface turbulence, small-scale roughness, near-surface temperature gradients, breaking waves, and the presence of surface active material, making parameterization a complicated task because these processes are as difficult to quantify under oceanic conditions as the gas fluxes themselves. Relating gas transfer velocities to an easily measured, fundamental quantity would help in developing accurate parameterizations of air-sea gas exchange.

[3] The air-sea flux, F (mol m^{-2} s^{-1}), of a sparingly soluble nonreactive gas can be expressed as

$$F = k_L(C_S - C_W) \quad (1)$$

where k_L (m s^{-1}) is the gas transfer velocity, C_S (mol m^{-3}) is the concentration of gas that would be expected in the water if the air and water were in equilibrium with respect to the partial pressure of the gas in the air, and C_W (mol m^{-3}) is the

[1]Air-Sea Interaction and Remote Sensing Department, Applied Physics Laboratory, University of Washington, Seattle, Washington, USA.
[2]Lamont-Doherty Earth Observatory, Columbia University, Palisades, New York, USA.
[3]Department of Civil and Environmental Engineering, School of Mining and Petroleum Engineering, University of Alberta, Edmonton, Alberta, Canada.

Corresponding author: W. E. Asher, Air-Sea Interaction and Remote Sensing Department, Applied Physics Laboratory, University of Washington, 1013 NE 40th St., Seattle, WA 98105, USA. (asherwe@apl.washington.edu)

0148-0227/12/2011JC007390

gas concentration in the bulk water. Sparingly soluble, nonreactive gases are termed liquid-phase rate controlled, and in this case k_L depends on hydrodynamics very near the surface in the aqueous phase. Surface divergence theory for the air-water transfer of a gas predicts that

$$k_L = a(D\beta_{RMS})^{1/2} \quad (2)$$

where a is a dimensionless constant, β_{RMS} (s^{-1}) is the RMS value of the divergence of the horizontal velocity fluctuations in the plane of the interface at the surface, and D ($m^2\ s^{-1}$) is the molecular diffusivity of the gas through water [*Banerjee and McIntyre*, 2004; *McCready et al.*, 1986; *Tamburrino and Gulliver*, 2002]. The surface divergence is defined as

$$\beta_{Surf} = -\frac{\partial w}{\partial z} = \nabla_H \cdot \vec{u} \quad (3)$$

where w is the vertical velocity and the divergence on the right-hand side is for the velocities in the plane of the air-water interface. In oceanographic applications, it is typical to rewrite (2) using the Schmidt number, Sc, of the gas in place of D (where Sc is defined as the kinematic viscosity, ν ($m^2\ s^{-1}$), divided by D). In this case, (2) is written as

$$k_L = b\left(\frac{\beta_{RMS}}{Sc}\right)^{1/2} \quad (4)$$

where the constant b has units of $m\ s^{-1/2}$ because it incorporates $\nu^{1/2}$.

[4] There have been several studies showing that equation (2) provides a general relationship for predicting k_L solely from hydrodynamic measurements [*Banerjee et al.*, 2004; *McKenna and McGillis*, 2004; *Tamburrino and Gulliver*, 2002; *Turney et al.*, 2005]. These studies have all relied on measuring β_{RMS} from surface particle-image velocimetry (PIV) measurements, where the motions of nearly neutrally buoyant particles with diameters on order of 100 μm are photographed and tracked. While these studies support the scaling of k_L implied by equation (2), it is difficult to envision PIV methods for measuring β_{RMS} would be practical for field applications. Use of surface divergence conceptual models for air-sea gas exchange would be possible if there were a simple, easily implemented method for estimating β_{RMS} at the ocean surface.

[5] It has been argued that infrared (IR) images of the water surface contain information concerning the surface flow field, including surface motions relating to air-water exchange [*Garbe et al.*, 2004; *Schimpf et al.*, 2004]. Therefore, IR imagery could provide a convenient means for estimating β_{RMS} that could be applied to air-sea exchange. However, there is no standard method for deducing β_{RMS} from such images. Here, we present results showing that determining the rate at which peaks are observed in a time series of the surface skin temperature measured by an IR imager can be used as an estimate of β_{RMS} for both wind-shear driven turbulence and mechanically generated turbulence. The estimates derived from the IR images are compared to velocity field divergences measured directly using PIV, β_{RMS}, and to independent estimates of β_{RMS} made using a surface laser-induced fluorescence technique [*Asher and Litchendorf*, 2009]. The estimates of β_{RMS} derived from the IR imagery are shown to scale with k_L values measured using gaseous tracers as predicted by equation (4) for both wind-driven and mechanically generated turbulence.

2. Experimental Procedure

[6] The experiments discussed here were performed in a synthetic jet array turbulence tank (SJAT) embedded in a wind tunnel (see Figure 1) previously described by *Asher and Litchendorf* [2009]. The SJAT is 0.5-m wide by 0.5-m long by 1-m deep tank mounted in a wind tunnel with a cross section of 0.5 m by 0.5 m and a test section length of 1.5 m. Turbulence in the aqueous phase is generated using an array of 16 pumps that are turned on and off in a random sequence as described by *Variano et al.* [2004]. The discharge velocity of each pump is a function of the pump drive voltage, P_V (V), which is the same for each of the 16 pumps. Each pump discharges through an opening that is 1 cm in diameter located 10 cm from the bottom of the tank with a discharge velocity calculated from the flow to be 45 cm s^{-1} for P_V = 12 V. The SJAT provides reproducible planar isotropic turbulence with intensity, Q (cm s^{-1}), that can be varied by changing P_V. Q is given by

$$Q = \sqrt{\frac{1}{3}\left(\bar{u}_x'^2 + \bar{u}_y'^2 + \bar{u}_z'^2\right)} \quad (5)$$

where $\bar{u}_x'$, $\bar{u}_y'$, and $\bar{u}_z'$ are the RMS turbulent velocity fluctuations in the x, y, and z (vertical) directions, respectively. Further details of the SJAT and its operation, including steps taken to reduce the effect of adventitious surface contamination, are provided by *Asher and Litchendorf* [2009].

[7] Q was measured at a depth of 1 cm as a function of wind speed, U (m s^{-1}), and P_V using the two-dimension digital particle-image velocimetry (PIV) method described below. Because the PIV provided only u_x' and u_z', the turbulence intensity from the PIV measurements is denoted Q_{PIV} and defined as

$$Q_{PIV} = \sqrt{\frac{1}{3}\left(2\bar{u}_x'^2 + \bar{u}_z'^2\right)} \quad (6)$$

where it has been assumed that the turbulence is isotropic in the plane of the air-water interface so that $\bar{u}_x' = \bar{u}_y'$ [*Variano et al.*, 2004]. In addition, Q was also measured at a water depth of 10 cm using an acoustic-Doppler velocimeter (ADV), Q_{ADV}, as described by *Asher and Litchendorf* [2009]. In the case of Q_{ADV}, the ADV provides all three velocity components so Q_{ADV} is calculated using equation (5).

[8] The PIV system imaged a 10-cm wide by 7.5-cm high by 2 mm thick region of water that was parallel to the wind vector, centered laterally in the SJAT, and included the air-water interface as shown in Figure 1. The light source was a dual-head Nd-YAG laser (Gemini PIV 90–30 Nd:YAG laser system, New Wave Research Inc., Fremont, California) producing 90 mJ of light with a 3 to 5 ns pulse width at a wavelength of 532 nm operating at a repetition rate of 30 Hz. A four-channel digital delay generator (model 500A, Berkeley Nucleonics, San Rafael, California) was used to control the timing of the laser light pulses. For these experiments, the pulse separation was set at 5 ms. A spherical lens with a focal length of 1000 mm and a cylindrical lens with a focal length

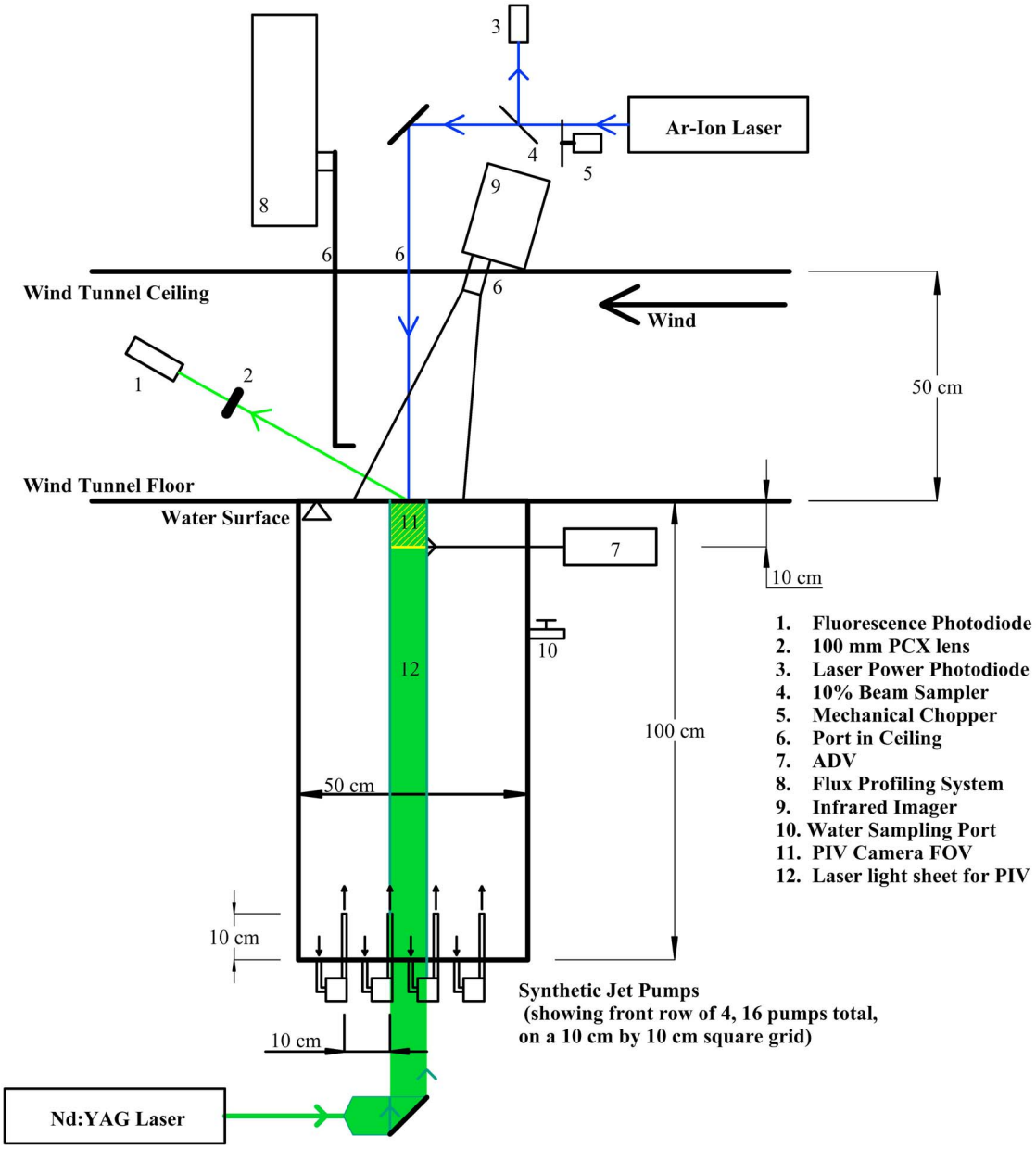

Figure 1. Schematic diagram of the experimental setup showing synthetic jet array tank (SJAT), particle image velocimetry (PIV) system, laser induced fluorescence (LIF) system, infrared imager, and flux profiling system.

of −19 mm were used to create a light sheet that was directing vertically upwards from the bottom of the SJAT using an external mirror. A monochrome, 2-megapixel (1,600 × 1,200 pixels) CCD digital video camera (DS-21-02M30-SA, DALSA, Waterloo, Ontario) using a Nikkor 180 mm f/2.8D (Nikon, Melville, New York) imaged the light sheet with a resolution of 0.0625 mm per pixel. The camera was positioned 24 cm below the mean water level looking up at an angle of 2.5° with respect to the horizontal. Images from the camera were recorded using a Pentium-IV class personal computer equipped with a DVR Express camera interface system (IO Industries, Inc., Canada) running Video Savant 4.0 (IO Industries, Inc., Canada). Using this system, 8-bit gray scale TIFF images from the camera could be recorded at frame rates up to 30 Hz. Conduct-O-Fil (Potters Industries, Valley Forge, Pennsylvania) silver-coated hollow glass spheres with a mean diameter of 15 μm provided the high reflectivity seed particles required for the PIV.

[9] Air temperature, T_{AIR} (K), and relative humidity, RH, in the wind tunnel were controlled using a dedicated air conditioner in the climate-controlled room. Wind speed, U (m s^{-1}), specific humidity, q (mol m^{-3}), and T_{AIR} were measured both along the centerline of the wind tunnel and 15 cm off the centerline, 10 cm upwind of the downwind

edge of the tank. Wind speed was measured using two pitot tubes, one fixed at a height of 33 cm above the water surface with a second mounted to a vertical linear traverse for collecting height profiles. The traversing pitot tube was located on the tank centerline and the fixed-height probe located 15 cm off the tank centerline. Differential pressure from each pitot tube was measured with a high precision pressure transducer (264, Setra Systems Inc., Boxborough, Massachusetts). *RH* and T_{AIR} were measured by the fixed height probe and the traversing probe. Each probe pumped air at a rate of 17 cm^3 s^{-1} through insulated tubes to separate water vapor analyzers (RH-300, Sable Systems, Las Vegas, Nevada). The resulting data for *RH* and T_{AIR} allow calculation of q from standard relations. T_{AIR} was also measured in the tunnel at the fixed and profiling heights using T-type thermocouples connected to thermocouple meters (TC-2000, Sable Systems, Las Vegas, Nevada). The profile measurements were performed at twelve measurement heights over a total distance of 30 cm with the lowest measurement height taken to be 0.5 cm above the largest waves in the tank. In a wind tunnel there is a second boundary layer region in the upper half of the tunnel associated with the wall-layer behavior from the ceiling. Therefore, close attention was paid such that the profile measurements were taken below the wake region influenced by the upper boundary layer. Determination of the friction velocity (u^*), latent heat flux, and sensible heat flux are made using the flux-profile relationships given by Monin-Obukhov similarity theory [*Edson et al.*, 2004].

[10] T_W was measured using three separate SBE-3 thermistors (Sea-Bird Electronics Inc., Bellevue, Washington), each with an accuracy of 0.001 K, at depths of 1 cm, 3 cm, and 10 cm, respectively. These sensors showed there was no thermal stratification in the bulk water.

[11] Spatial and temporal variations in water surface skin temperature, T_S (K), were measured using a mid-wave IR imager (Radiance HS, Raytheon TI Systems, Houston, Texas) calibrated using a blackbody source (Model 2004S, SBIR, Santa Barbara, California). The imager was mounted above the wind tunnel looking downward at an incidence angle of 5° and a field of view of 60° through a 4-cm diameter port in the top panel. For this geometry the imager field of view was the entire tank surface, with a spatial resolution of approximately 0.2 cm by 0.2 cm per pixel. The imager measured T_S with a precision of 0.05 K at a frame rate of 120 Hz. Further details concerning the IR imager and its data collection system are provided by *Asher et al.* [2004].

[12] Temporal fluctuations in the aqueous-phase concentration of CO_2 at the water surface were measured using the laser-induced fluorescence (LIF) technique described by *Asher and Litchendorf* [2009]. The technique uses the pH-sensitive fluorescent dye 2′,7′-dichlorofluorescein (DCFS) to track changes in pH within 300 μm of the water surface caused by the water-to-air flux of CO_2. The LIF sampling area was a 5-mm diameter circle located in the middle of the field of view of the IR imager. Surface fluorescence intensities and incidence laser power levels were sampled at a rate of 100 Hz using a lock-in detection scheme. The raw intensities were then corrected to account for changes in fluorescence due to fluctuations in incident laser intensity, with the power-corrected fluorescence intensities converted to pH using a calibration curve generated by measurements of bulk tank water pH, which was adjusted to a nominal value of 4.9 at the start of each experiment. Further details of the experimental configuration of the LIF measurements are provided by *Asher and Litchendorf* [2009].

[13] Gas transfer velocities were measured for evasion of helium (He) and sulfur hexafluoride (SF_6) by sampling the bulk tank water. Dissolved gas concentrations in the bulk water were measured by taking 30 cm^3 samples at intervals ranging from 1800 s to 3600 s, depending on P_V and U as described by *Asher and Litchendorf* [2009]. The aliquot samples were then analyzed for dissolved gas concentration using the headspace method of *Wanninkhof et al.* [1987]. The rate of change of concentration was then used to estimate k_L following the method outlined by *Asher et al.* [1996].

[14] Two series of experiments were carried out in the SJAT. The first was a study of the effect of changes in U at constant P_V, with the latter set at 14 V. The second series of measurements looked at the effect of changing P_V at constant U, with the latter held at 3.2 m s^{-1}. The conditions used for each set of experiments, as well as the environmental data for each run are listed in Table 1. (Henceforth, the term "pump-forced" will be used to denote the group of experiments done at a constant wind speed with variable pump voltage. In contrast, "wind-forced" will be used to denote the set of experiments where pump voltage was kept constant and variable wind speed.)

[15] Small scale waves were generated when $U > 3.2$ m s^{-1} for the wind-forced experiments. These waves cause the image of the fluorescence to move across the active area of the photodetector, leading to large fluctuations in signal that were not correlated with changes in CO_2 concentration. Therefore, the LIF technique was not used during the wind-forced experiments. In contrast, the IR imager was not affected by the waves since the focal plane array of the imager was much larger than their wavelength.

3. Data Analysis and Results

[16] Two-dimensional velocity fields were estimated from the PIV images using a cross-correlation algorithm based on that developed by *Willert and Gharib* [1991]. This basic scheme was modified to incorporate an iterative-multigrid algorithm [*Scarano and Reithmuller*, 2000], a Gaussian digital masking technique [*Gui et al.*, 2001] to reduce the uncertainty of estimation, and a universal outlier detection algorithm [*Westerweel and Scarano*, 2005] for the detection of spurious vectors. Briefly, displacement fields were calculated for each image pair by iteratively tracking groups of particles between the interrogation window in the first image and the corresponding search window in the second image. The most likely positions of identical particles in the two images were determined by locating the cross-correlation peak across multiple grids of interrogation and search windows. The algorithm first estimated the displacement fields using interrogation windows of 64 pixels by 64 pixels. The coarse result was used as a predictor of the flow field for a refined flow field estimate using windows that were 32 pixels by 32 pixels where the locations of the search and interrogation windows were determined from the coarse flow field. A 50% window overlap was then used on the refined estimate to increase the spatial resolution to

Table 1. List of Experimental Conditions Studied and Relevant Data for Constant Pump Voltage With Variable Wind Speed (Wind-Forced) and Variable Pump Voltage and Constant Wind Speed (Pump-Forced)[a]

U (m s^{-1})	P_V (V)	RH (%)	T_A (°C)	T_W (°C)	Q_{PIV} (cm s^{-1})	Q_{ADV} (cm s^{-1})	u^* (m s^{-1})	$k_{He}(660)$ (cm h^{-1})	$k_{SF6}(660)$ (cm h^{-1})	n_i	s_{TS} (s^{-1})	s_{pH} (s^{-1})	β_{RMS} (s^{-1})
Wind-Forced P_V Constant, U Variable													
3.2	14	34.2	21.2	22.9	7.98	7.10	0.083	9.43	n.a.	n.a.	0.17	n.a.	7.79
5.6	14	35.8	23.0	22.5	6.41	6.71	0.21	14.7	13.7	0.54	0.44	n.a.	3.18
7.0	14	33.9	22.9	22.2	3.84	4.88	0.25	17.3	19.6	0.43	1.11	n.a.	2.60
7.9	14	33.5	22.7	22.1	6.82	6.97	0.36	23.4	23.0	0.51	1.54	n.a.	3.58
Pump-Forced P_V Variable, U Constant													
3.2	10	34.7	19.1	21.0	4.18	4.58	0.12	10.3	11.2	0.51	0.50	0.22	3.91
3.2	10	40.2	19.4	21.1	4.18	4.58	0.12	12.2	13.4	0.50			
3.2	10	39.4	19.6	21.5	4.18	4.58	0.12	13.2	12.7	0.57			
3.2	14	31.7	19.5	21.7	7.60	7.89	0.14	17.7	16.3	0.60	0.80	0.36	6.17
3.2	14	35.9	19.5	21.6	7.60	7.89	0.10	17.5	17.4	0.55			
3.2	14	37.4	19.8	21.7	7.60	7.89	0.12	16.5	16.6	0.55			
3.3	16	31.6	19.1	21.7	9.26	9.26	0.12	21.1	20.3	0.57	1.07	0.45	7.73
3.2	16	40.7	19.3	21.8	9.26	9.26	0.11	17.9	17.0	0.58			
3.2	18	34.0	19.1	22.2	10.30	10.47	0.12	22.3	20.6	0.59	1.38	0.51	9.81
3.2	18	34.2	19.6	22.4	10.30	10.47	0.12	20.3	23.6	0.47			
3.3	18	38.7	19.5	22.2	10.30	10.47	0.12	20.8	21.5	0.53			
3.2	20	31.6	19.2	22.2	12.86	11.77	0.13	25.4	25.2	0.55	1.84	0.69	15.6
3.2	20	37.7	19.3	22.4	12.86	11.77	0.10	23.1	22.9	0.56			

[a]Wind speed, U; pump voltage, P_V; relative humidity, RH; air temperature, T_A; water temperature, T_W; turbulence intensity from PIV, Q_{PIV}; turbulence intensity from ADV, Q_{ADV}; air-side friction velocity, u^*; gas transfer velocity for He, $k_{He}(660)$; gas transfer velocity for SF_6, $k_{SF6}(660)$; Schmidt number exponent, n_i, defined in equation (8); peak rate of surface temperature fluctuations, s_{TS}; peak rate of surface pH fluctuations, s_{pH}; and RMS surface divergence computed from PIV, β_{RMS}.

16 pixels by 16 pixels, providing velocity measurements to within approximately 1 mm the air-water interface. Typically, fewer than 4% of the velocity vectors were detected as spurious. The uncertainty in the velocities was estimated to be on order of ± 0.2 cm s^{-1}.

[17] Figure 2 shows Q_{PIV} measured at a depth of 1 cm plotted as a function of U with P_V equal to 14 V and Figure 3

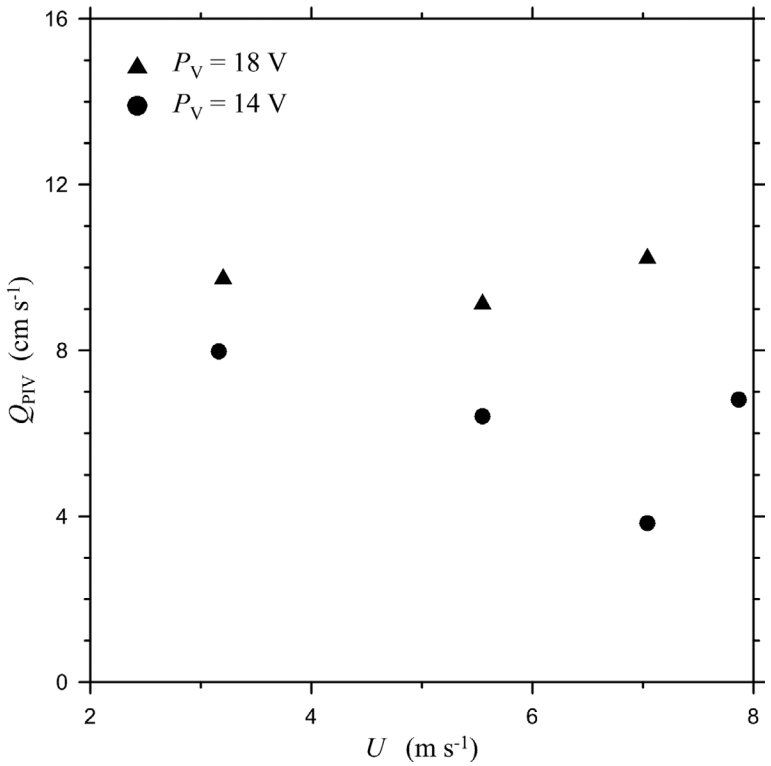

Figure 2. Turbulence intensity at a depth of 1 cm derived from the PIV, Q_{PIV}, as defined in equation (6) versus wind speed, U, at pump voltages, P_V, of 14 V and 18 V (i.e., the wind-forced case).

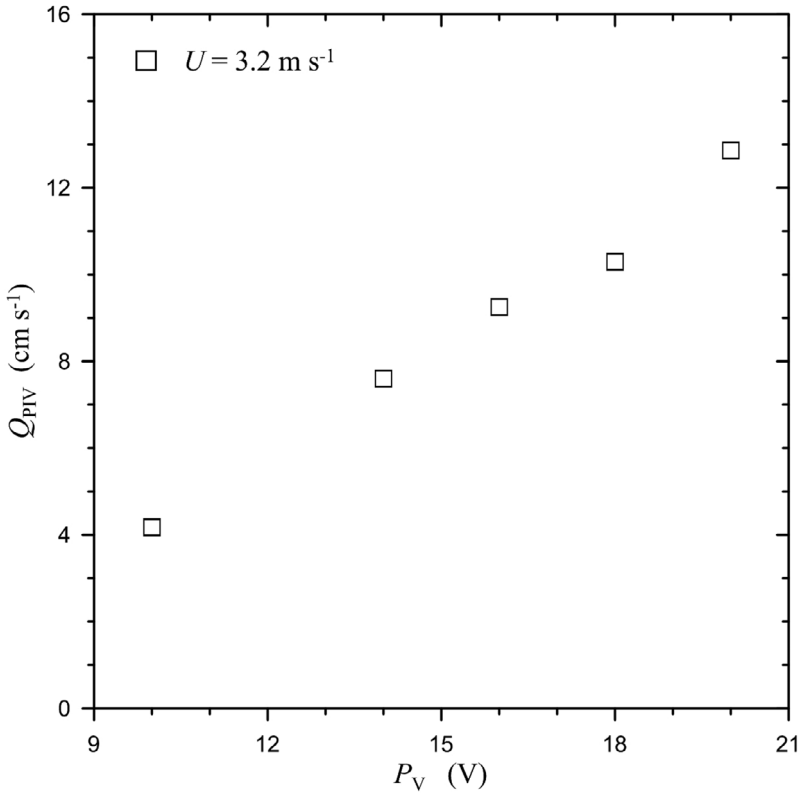

Figure 3. Turbulence intensity at a depth of 1 cm derived from the PIV, Q_{PIV}, as defined in equation (6) versus pump voltage, P_V, for wind speed, U, equal to 3.2 m s^{-1} (i.e., the pump-forced case).

shows Q_{PIV} measured as a function of P_V for U equal to 3.2 m s^{-1}. As might be expected, the data for the pump-forced case in Figure 3 show that Q_{PIV} increases linearly with increasing P_V. In contrast, the data in Figure 2 for the wind-forced case indicate there is little or no correlation between Q_{PIV} and U. As corroboration that the turbulence intensities in Figure 2 and Figure 3 are accurate, Figure 4 shows Q_{PIV} plotted versus Q_{ADV} where the ADV data were collected concurrently with the PIV data.

[18] Figure 5 shows the friction velocity, u^* (m s^{-1}), determined from the air-side flux profile measurements made concurrently with the turbulence measurements in Figure 2. This figure shows u^* increases with U despite the lack of correlation between Q_{PIV} with U. While the PIV data for the wind-forced case is discussed in detail in the following section, in general, the data in Figures 2–5 show that turbulence in both the air and water in the SJAT increased with the external forcing from the pumps and wind.

[19] The RMS horizontal divergence as defined in equation (3), β_{RMS} (s^{-1}), was determined from the PIV data by calculating the vertical gradient of the vertical velocity fluctuations over a depth range of 0.5 cm to 1 cm. Although *McKenna* [2000] has shown that for a clean water surface the divergence measured at this depth is not identical to the true surface divergence defined in equation (3), *McKenna* [2000] also demonstrated that the two values are correlated. Therefore, it will be assumed here that the PIV data from 0.5 cm can be used as an estimate of the true surface divergence. Figure 6 shows β_{RMS} derived from the PIV velocity fields plotted as a function of Q_{PIV} for both the pump-forced and wind-forced cases. Regardless of the forcing mechanism, the surface divergence increases with increasing Q_{PIV}.

[20] The spatial scales of the surface temperature measurements provided by the imager were matched to the spatial scales of the LIF measurements by selecting a 3 by 3 pixel region of the 256 by 256 image centered on the location of the LIF measurement. The T_S values for these nine pixels were then averaged to provide a surface temperature corresponding to approximately the same area as the LIF measurement. However, LIF and IR data could not be collected simultaneously because the argon-ion laser heated the water surface by a few tenths of a Kelvin. Although this increase did not affect the surface hydrodynamics it was visible in the IR images and prevented collecting LIF and IR imagery data simultaneously.

[21] Time series for T_S and pH for U = 3.2 m s^{-1} and P_V = 18 V that have both been low-pass filtered with a cutoff frequency of 15 Hz are shown in Figure 7 (see *Asher and Litchendorf* [2009] for details of the filtering method). Although the data for T_S and pH were not taking simultaneously, they are similar in that both show a relatively constant baseline value with a series of peaks with approximately the same width and frequency of occurrence. In the case of pH, the peaks represent times when pH increased at the water surface and in the case of T_S the peaks represent periods when the water surface cooled (T_S is plotted with a descending y axis). This qualitative similarity reflects

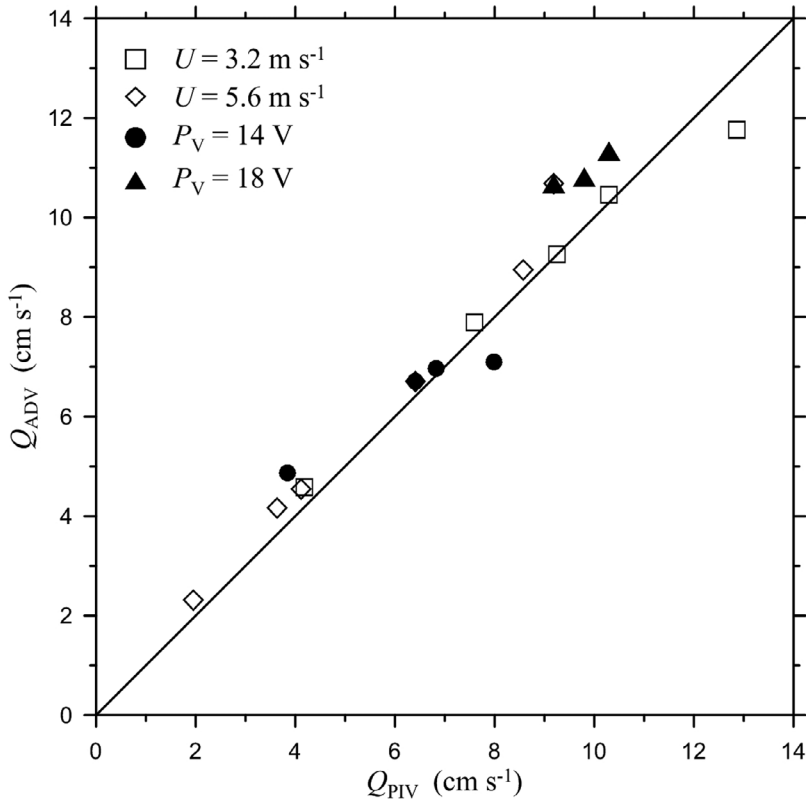

Figure 4. Turbulence intensity at a depth of 1 cm as derived for the PIV measurements, Q_{PIV}, versus turbulence intensity at a depth of 10 cm measured by the ADV, Q_{ADV}.

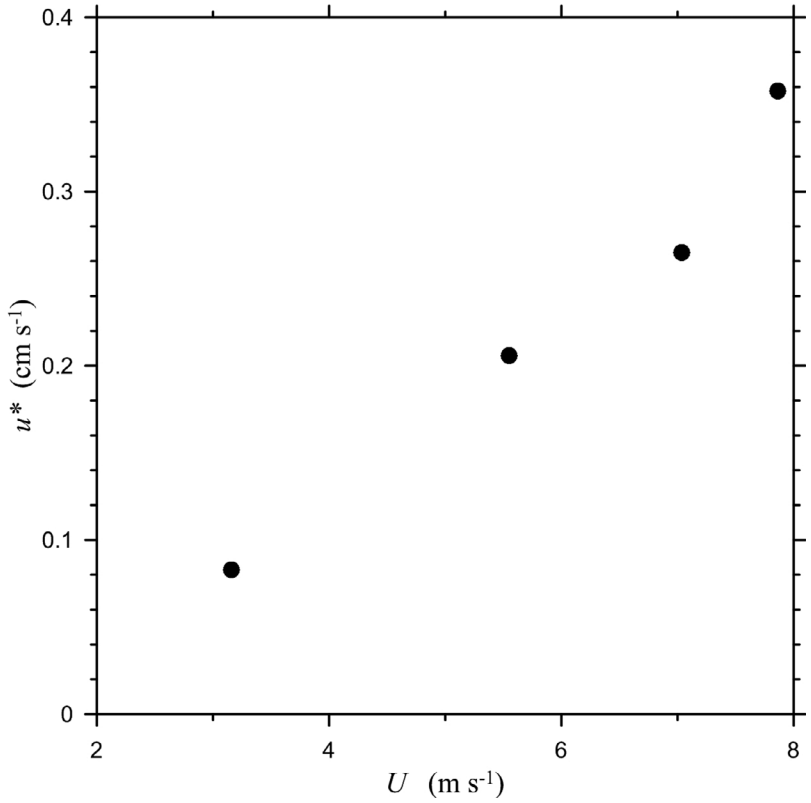

Figure 5. Friction velocity, u^*, determined by the gradient flux profiling system versus wind speed, U.

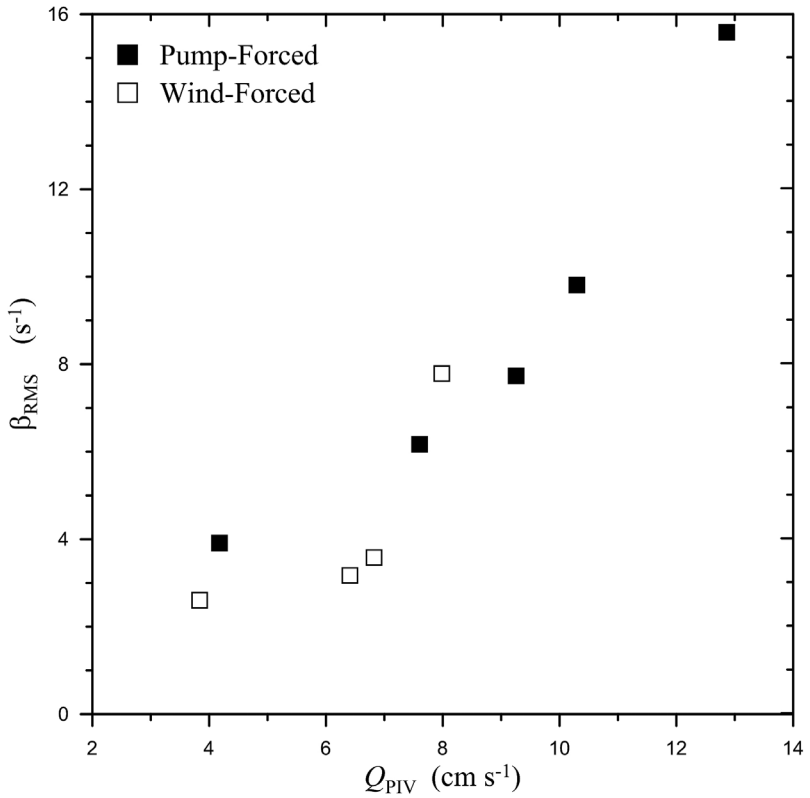

Figure 6. RMS surface divergence, β_{RMS} (s^{-1}), determined from the PIV data for the SJAT versus turbulence intensity determined from the PIV data, Q_{PIV}, for conditions where wind speed, U, was held constant at 3.2 m s^{-1} and pump voltage, P_V, varied and conditions where P_V was held constant and U varied. Data key is shown in the figure.

that they share a common generation mechanism related to a net air-water flux and the aqueous-phase hydrodynamics very near the water surface.

[22] A peak detection program [*Asher and Litchendorf*, 2009] was used to measure peak widths in the time series for pH and T_S, τ_{pH} (s) and τ_{TS} (s), respectively. From these data, distributions of τ_{pH} and τ_{TS} were calculated as a function of Q_{PIV} in the case of pH and as a function of Q_{PIV} and U for T_S. Figure 8 shows the distribution of τ_{pH} calculated from time series of pH, $p(\tau_{pH})$ (s^{-1}), for two pump-forced conditions (Q_{PIV} = 10.3 cm s^{-1} and Q_{PIV} = 4.18 cm s^{-1}). These distributions closely resemble those reported by *Asher and Pankow* [1989] using a similar LIF method for a grid-stirred tank in the absence of wind-forcing. Also shown in Figure 8 are distributions of τ_{TS}, $p(\tau_{TS})$ (s^{-1}), calculated from the time series for T_S under the same conditions as pH. For a given value of Q_{PIV}, $p(\tau_{pH})$ and $p(\tau_{TS})$ have similar shapes, although the mode of the distributions generated from the temperature data is smaller than the mode of the distributions generated from the pH data.

[23] The rate at which divergence events in pH or T_S was observed, s_{pH} (Hz) and s_{TS} (Hz), respectively was calculated as total number of peaks in pH or T_S detected over a given time period divided by that time. Figure 9 shows s_{pH} (Hz) and s_{TS} (Hz) plotted as a function of forcing mechanism in the SJAT. Figure 9 (left) shows s_{TS} for the wind-forced experiments (as discussed above LIF measurements were not possible for the wind-forced case due to the presence of small-scale waves at higher wind speeds). Figure 9 (right) shows s_{TS} and s_{pH} plotted as a function of Q_{PIV} for the pump-forced data set. Both s_{TS} and s_{pH} increase as the intensity of the forcing increases, with $s_{TS} > s_{pH}$ at a given value of Q_{PIV}. As discussed in detail in the next section, this behavior can be explained in terms of the difference between the diffusive length scale of heat and of gases.

[24] Figure 10 shows bulk air-water gas transfer velocities measured in the SJAT using He and SF_6. In Figure 10, the transfer velocities have been corrected to Sc = 660 by assuming that

$$k_{He}(660) = k_{He}(\text{meas.})\left(\frac{\text{Sc(He)}}{660}\right)^{n_{AVG}}$$
$$k_{SF6}(660) = k_{SF6}(\text{meas.})\left(\frac{\text{Sc(SF}_6\text{)}}{660}\right)^{n_{AVG}} \quad (7)$$

where k_{He}(meas.) and k_{SF6}(meas.) are the measured transfer velocities of He and SF_6, respectively, Sc(He) and Sc(SF_6) are the Schmidt numbers of He and SF_6 at T_W, respectively, and n_{AVG} is the average Schmidt number exponent for that set of conditions defined as

$$n_{AVG} = \frac{1}{N_T}\sum_i n_i = \frac{1}{N_T}\sum_i \frac{\ln\left(k_{SF6,i}(\text{meas.})/k_{He,i}(\text{meas.})\right)}{\ln\left(\text{Sc(He)}_i/\text{Sc(SF}_6)_i\right)} \quad (8)$$

where N_T is the number of individual experiments done at a particular combination of P_V and U and the summation

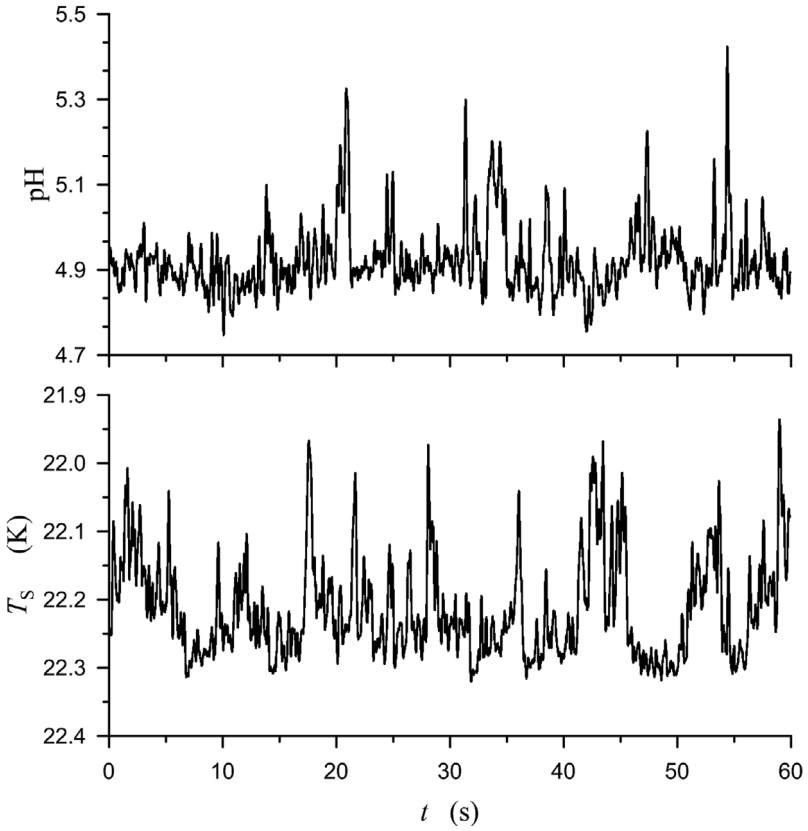

Figure 7. Time series of (top) water surface pH measured using laser-induced fluorescence and (bottom) water surface temperature, T_S, measured by the infrared imager. T_S has been plotted with a descending y axis so that each peak in its time series represents a cooling event. Experimental conditions were wind speed, U, equal to 3.2 m s^{-1} and aqueous-phase turbulence intensity measured by particle-image velocimetry, Q_{PIV} (see equation (6)), equal to 10.5 cm s^{-1}. Note that although the total time in each series is the same, the data were not taken simultaneously.

is over all experiments done under those conditions. Equation (8) is derived from equation (4) where the exponent $-1/2$ is replaced by $-n$. Figure 10 (left) shows $k_{He}(660)$ (cm h^{-1}) and $k_{SF6}(660)$ (cm h^{-1}) plotted versus U for the wind-forced data. Figure 10 (right) shows $k_{He}(660)$ and $k_{SF6}(660)$ plotted as a function of Q_{PIV} for the pump-forced data. The experimental uncertainty was similar for He and SF_6 and is shown only for $k_{He}(660)$. Table 1 provides $k_{He}(660)$, $k_{SF6}(660)$, and n_i for the data in Figure 10, which show that k_L increases with increases in either U or P_V.

4. Discussion

[25] The LIF method measures the fluorescence emitted from the water surface. However, the fluorescence intensity decreases exponentially with depth so that 90% of the total measured fluorescence signal is emitted between depths of 0 μm and 300 μm [*Asher and Litchendorf*, 2009]. As will be shown below, the time scale of the peaks in pH is approximately 0.3 s, which corresponds to a diffusive length scale for CO_2 of O(10 μm). This means that the layer of water for which the pH is elevated above the bulk value of 4.9 is, on average, much thinner than the fluorescence probe depth. This is supported by the observation that the LIF-measured pH is approximately 4.9 for a significant fraction of time, which implies that during that time the top 300 μm of the water surface has a pH that is not elevated and close to the bulk pH.

[26] The presence of the peaks in pH (or fluorescence intensity) and temperature can be explained through a surface divergence/convergence model of flow very near the water surface. Under most conditions, the concentration profile for CO_2 near the water surface is as shown at P_1 in Figure 11, with a very steep gradient in CO_2 near the surface. However, that thin layer gets swept downward in convergence zones, so that what was a thin layer of low-CO_2, high-pH water very near the surface becomes a downward moving column of low-CO_2, high-pH water spanning the fluorescence interrogation region as shown at P_2. Therefore, the peaks in pH (or fluorescence) in Figure 7 represent convergences at the water surface. Furthermore, by continuity their statistics will be directly related to the statistics of the divergences postulated to control air-water transfer. Because the CO_2 gradient is very near the surface, the streamlines of the convergence events must also extend close to the surface if they are to sweep high-pH water downward to generate a measurable peak in fluorescence and pH.

[27] The time series for T_S is similar to that for pH in that there is a relatively constant background value for T_S with

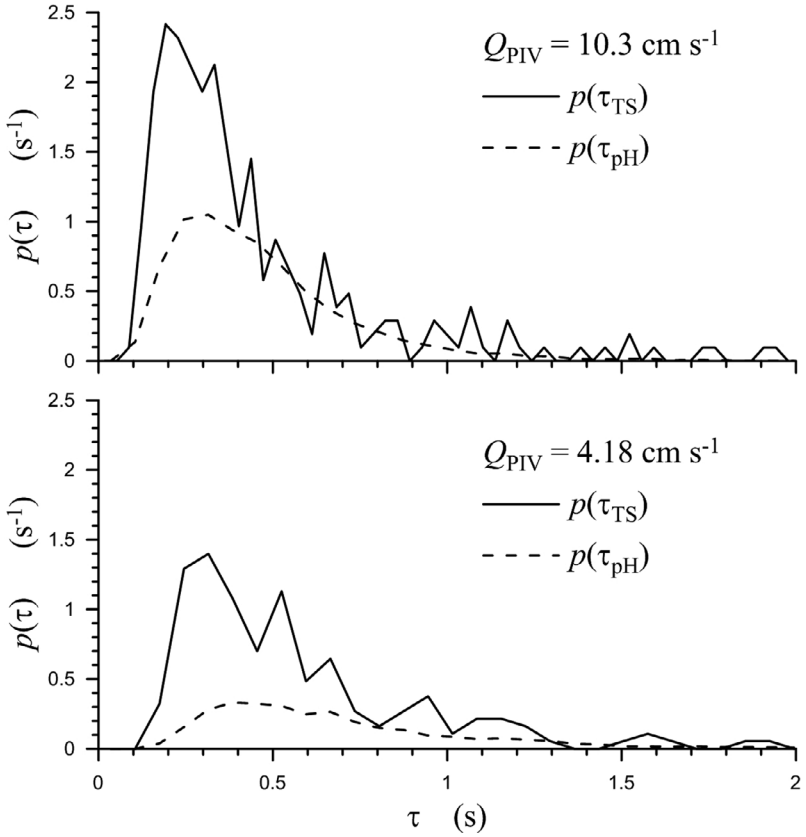

Figure 8. Distributions of time scales measured in the SJAT using temperature and LIF for two pump-forced conditions with (top) Q_{PIV} = 10.3 cm s^{-1} (P_V = 18 V, U = 3.2 m s^{-1}) and (bottom) Q_{PIV} = 4.18 cm s^{-1} (P_V = 10 V, U = 3.2 m s^{-1}).

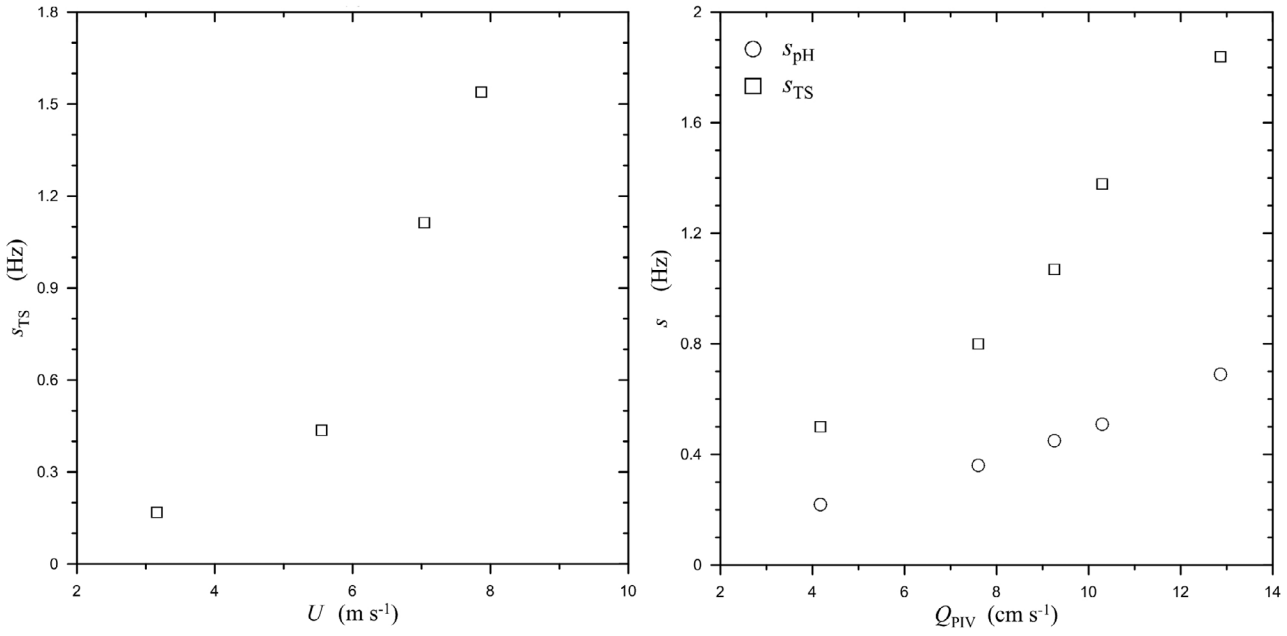

Figure 9. Peak rate determined from analysis of time series of pH fluctuations, s_{PH}, or from time series of temperature fluctuations, s_{TS}, using the procedure described by *Asher and Litchendorf* [2009]. Plot at left shows s_{TS} plotted versus wind speed, U, at a constant pump voltage of 14 V, and plot at right shows s_{PH} and s_{TS} plotted versus Q_{PIV} at a constant U of 3.2 m s^{-1}.

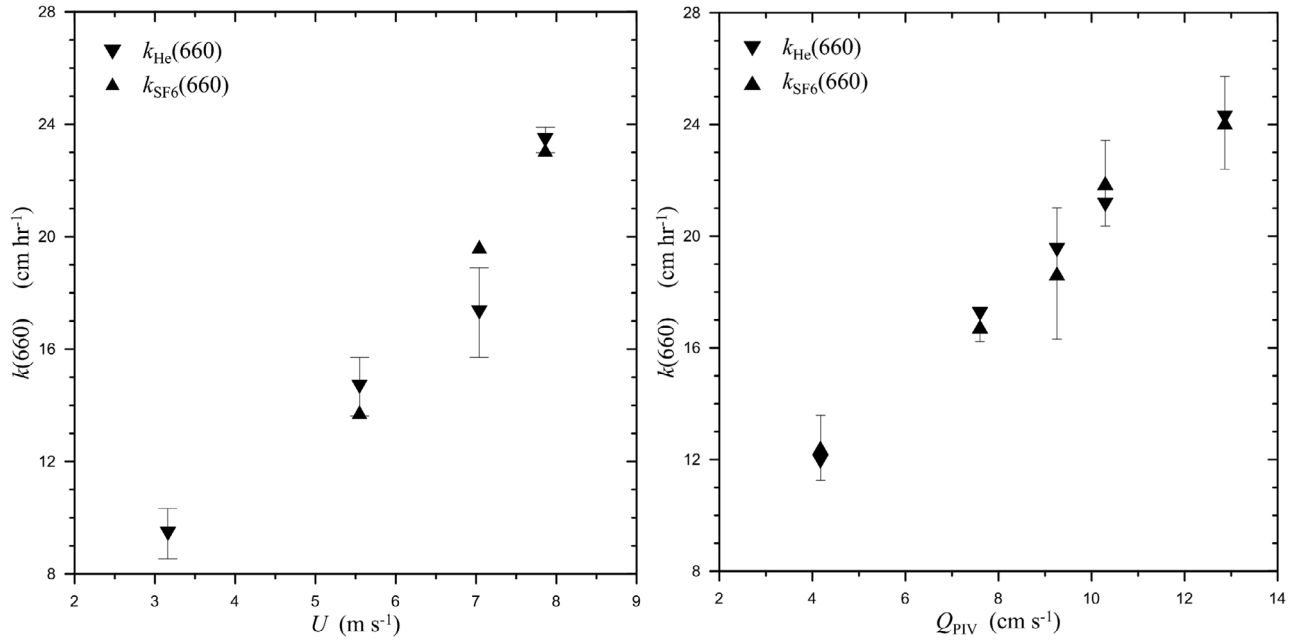

Figure 10. Air-water gas transfer velocities of helium (He) and sulfur hexafluoride (SF_6), $k_{He}(660)$ and $k_{SF6}(660)$ (where the 660 signifies that transfer velocities have been normalized to a Schmidt number of 660 using equation (7)), measured in the SJAT. Plot at left shows $k_{He}(660)$ and $k_{SF6}(660)$ as a function of wind speed, U, at a constant pump voltage, P_V, of 14 V (i.e., wind-forced). Plot at right shows $k_{He}(660)$ and $k_{SF6}(660)$ as a function of pump voltage, P_V, at a constant wind speed, U, of 3.2 m s^{-1} (i.e., pump-forced). The experimental uncertainties for He are shown as the error bars.

narrow spikes. However, these T_S events are in the opposite direction from pH, with rapid decreases in T_S observed. Because the net heat flux was from the water to the air, the water surface was cooling and the mechanism generating the decreases in T_S is identical to that for pH. The downward peaks in T_S therefore represent times when convergences swept cooler water from very near the surface downward. However, the interplay between effective radiative depth and the diffusivity of heat leads to a difference in the near-surface gradients for heat and gas.

[28] Over the wavelength range relevant to the IR imager used here (i.e., 3 μm to 5 μm), 90% of the IR photons measured by the imager originate from a layer that is approximately 200 μm thick [*Irvine and Pollack*, 1968]. This means the temperature measured by the imager is integrated over a depth that is comparable to that of the fluorescence

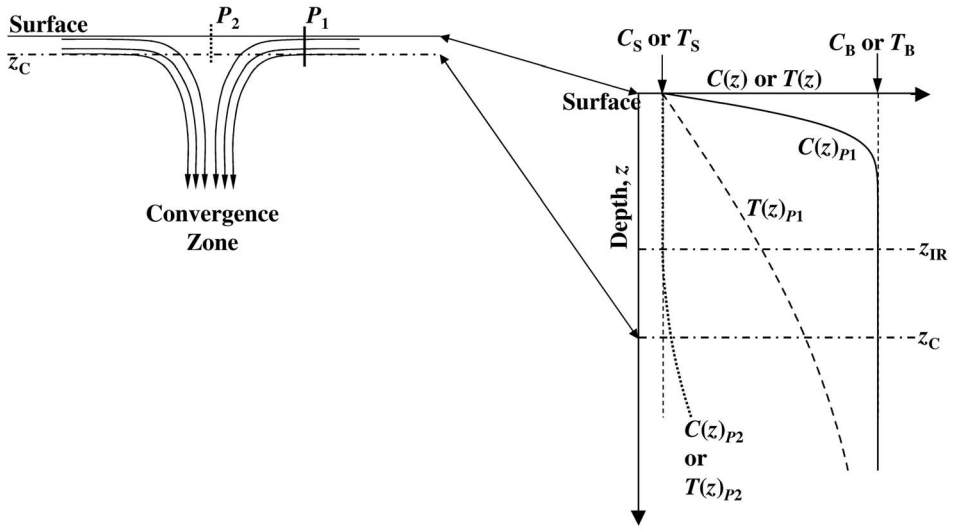

Figure 11. Schematic diagram showing how a convergence event leads to the peaks in pH and temperature shown in Figure 7. Note that concentration is inversely related to pH because CO_2 is an acid, and a CO_2 concentration decrease leads to an increase in pH.

measurement depth. Also in similarity with the water-to-air flux of CO_2 that creates the pH gradient, the net water-to-air heat flux is driven mainly by the latent heat flux at the air-water interface and not radiative transfer from deeper in the surface layer. The result is that the vertical gradient for temperature has a profile that is similar to the vertical gradient for CO_2. However, the molecular diffusivity of heat is approximately two orders of magnitude larger than the diffusivity of CO_2 so that for a time scale of 0.3 s the diffusive length scale for heat is approximately 200 μm. This means that as the water surface cools, the heat from below can diffuse upwards and the gradient for temperature at the surface will therefore be less steep than for CO_2 but will extend to larger depths than the gradient for CO_2. Convergence streamlines would therefore not have to be as close to the surface to cause a decrease in the measured temperature. If there is a depth-dependence to the divergences as postulated by *Brumley and Jirka* [1988], this difference between heat and CO_2 implies that the rate that peaks in temperature occur will be different than the rate for peaks in pH. In a sense, these depth-dependent convergences are the surface penetration events of penetration theory as formulated by *Harriott* [1962] and applied by *Atmane et al.* [2004].

[29] In the absences of other data, the plot of Q_{PIV} versus U shown in Figure 2 would indicate that near-surface turbulence in the SJAT was independent of U. However, there are several pieces of independent evidence demonstrating that near-surface turbulence increased with U: Figure 5 shows that u^* increased with increasing U; Figure 9 (left) shows that s_{TS} increased with increasing U; and Figure 10 (left) shows k_L increased with increasing U. Because k_L, u^*, and s_{TS} are all controlled by turbulence at the water surface, their increase with U shows that wind speed affected water-side hydrodynamics, even if those effects could not be measured by the PIV at a depth of 1 cm as implied by the lack of correlation between Q_{PIV} and U in Figure 2. The most likely explanation for this lack of correlation is that the wind-driven boundary layer at the water surface had not developed enough in the relatively short fetch of the SJAT to affect the velocity measured using the PIV at a depth of 1 cm [*Caulliez et al.*, 2007].

[30] In contrast to Q_{PIV}, s_{TS} is measured at the surface and is correlated with both U for the wind-forced case and with P_V for pump-forced case (see Figure 9, which also shows that s_{pH} is correlated with P_V for the pump-forced case). However, in order for s_{pH} and s_{TS} to be useful for addressing air-water exchange, it must be demonstrated that they are related to the RMS surface divergence, β_{RMS}, required for use in equation (2) or equation (4). The problem in relating either convergence rate to the surface divergence is that although β_{RMS} has dimensions of frequency it does not describe the temporal scale of a process but instead is an area-extensive property derived from the two-dimensional velocity field at the surface. Relating β_{RMS} to s_{pH} or s_{TS} requires assuming that the temporal fluctuations observed at a point are related to the spatial properties of the flow field observed over a broad area.

[31] Figure 12 shows s_{pH} and s_{TS} plotted versus β_{RMS} determined from the PIV data where each was measured for the pump-forced turbulence. The data show that both rates are linearly correlated with the measured divergence. This suggests that because s_{pH} and s_{TS} are measured at the surface, they not only provide estimates of β_{RMS} but also could be used to estimate gas transfer velocities. More important, there is a difference in the slopes of the linear correlation between s_{pH} and β_{RMS} and s_{TS} and β_{RMS}. This difference in the convergence rate as a function of the surface divergence suggests that although both s_{pH} and s_{TS} are related to β_{RMS}, there is a depth-dependence to the near-surface flow associated with the convergences. In other words, there exist divergence/convergence events that have a measurable effect on surface temperature but do not affect the near-surface gas concentration profile. This observation is consistent with the evidence for partial surface renewal events reported by *Jessup et al.* [2009].

[32] *Variano and Cowen* [2008] and *Janzen et al.* [2010] have shown that the turbulence velocities very near the interface in a mechanically stirred tank decay rapidly toward the surface. Although this behavior does not agree with theoretical predictions concerning the behavior of turbulence near a clean water surface, it is similar to modeling results for turbulence near a solid boundary [*Magnaudet and Calmet*, 2006]. *Variano and Cowen* [2008] argue that this similarity between the model results for a solid boundary and the laboratory data for air-water interfaces arises because of adventitious contamination of the water surface. The water surface in the SJAT was continually cleaned using the pipette vacuuming technique [*Asher and Litchendorf*, 2009; *Kou and Saylor*, 2008], but given the difficulty of performing gas transfer experiments with water surfaces known to be free of surfactants [*Frew et al.*, 2004], even the vacuuming in the SJAT does not guarantee that turbulence near the water surface would behave as it would next to a perfectly clean air-water interface. If it is assumed that the water surface in the SJAT was impacted to some extent by surface contamination, turbulence velocities would decrease with depth near the air-water interface. This vertical structure causes the divergence to decrease near the water surface [*Magnaudet and Calmet*, 2006]. If there is a depth dependence to the divergences, so that not every divergence and convergence extends through the surface layer to the air-water interface, the convergences at greater depth will have a greater effect on T_S than on pH (since the gradient for temperature extends to larger depths than the gradient for CO_2 concentration (and therefore pH) as shown in Figure 11). If the depth of a convergence event is defined as the depth of the topmost layer with a nonzero velocity in the direction of the convergence, it is reasonable to assume there would be more convergence events that occur farther away from the interface. Therefore, the probability of detecting a convergence in the time series should be greater for T_S than in the data for pH. Furthermore, if the horizontal velocity decays to zero some distance from the interface, then the slower velocities nearer the surface should cause the convergence events for pH to have longer time scales than the convergence events for T_S.

[33] The measured distributions of τ_{TS} and τ_{pH} in Figure 8 support the hypothesis that the depths of the divergence and convergence events are not constant and do not completely renew the air-water interface (i.e., if complete renewal predominated, then the distributions for τ_{TS} and τ_{pH} would the same). For example, the convergence rate distributions for Q_{PIV} = 10.3 cm s^{-1} in Figure 8 show that the maximum value of $p(\tau_{TS})$ is a factor of 2.3 larger than the maximum value of $p(\tau_{pH})$ and the two modes occur at time scales

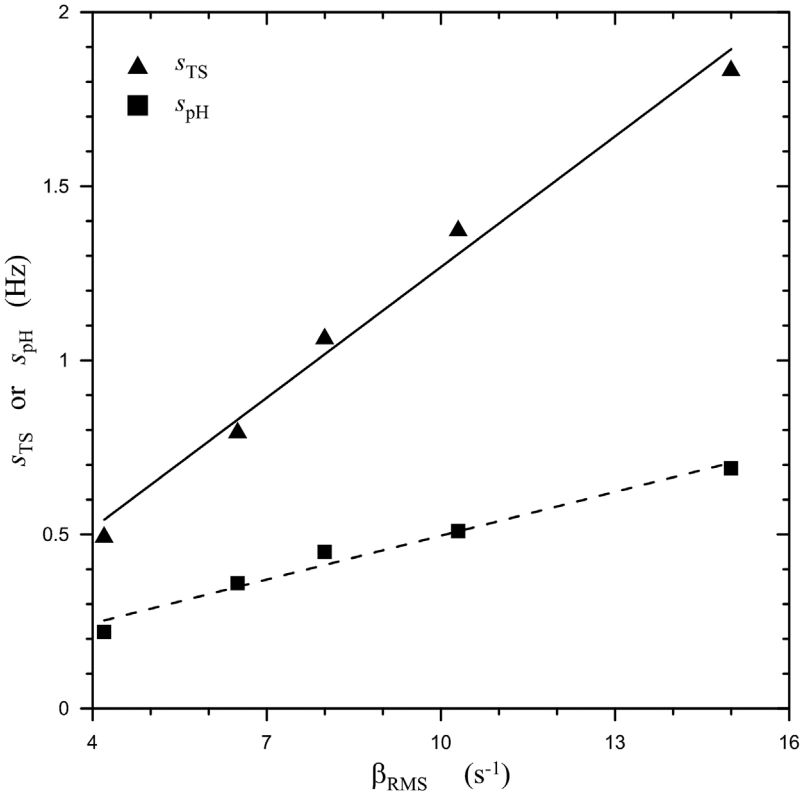

Figure 12. The rate at which convergence events are observed in surface temperature and pH, s_{Ts} and s_{TS}, respectively, plotted versus the RMS divergence, β_{RMS}, measured at a depth of 1 cm using the PIV. Data shown are for turbulence generated as a function of pump voltage at a constant wind speed, U, of 3.2 m s^{-1} (i.e., pump-forced).

of 0.20 s ($p(\tau_{TS})$) and 0.32 s ($p(\tau_{pH})$). Similarly, for Q_{PIV} = 4.18 cm s^{-1} the maximum value of $p(\tau_{TS})$ is a factor of 4.2 larger than the maximum value of $p(\tau_{pH})$ and the modes occur at time scales of 0.32 s ($p(\tau_{TS})$) and 0.39 s ($p(\tau_{pH})$), respectively. Based on these data, there are more convergence events overall for temperature, and they have slightly faster time scales on average, than the convergence events detected using pH and the LIF technique. Therefore, the statistics of the convergence events support the contention that there is a depth-dependence to the divergences thought to control air-water transfer.

[34] The analysis above provides evidence that s_{pH} and s_{TS} are related to the RMS surface divergence. Therefore, either s_{pH} or s_{TS} could be used as proxies for β_{RMS} in equation (4) to calculate k_L. This implies that k_L measured in the SJAT should scale linearly with the square root of s_{pH} or s_{TS} regardless of whether the primary forcing for gas transfer is due to the mechanically generated turbulence from the pumps or the surface wind stress. Figure 13 shows the average of $k_{He}(660)$ and $k_{SF6}(660)$ measured at the same U and P_V, $k_{Gas}(660)$, plotted versus $s_{TS}^{1/2}$ for the pump-forced and wind-forced data sets listed in Table 1. Also shown are $k_{Gas}(660)$, plotted versus $s_{pH}^{1/2}$ for the pump-forced data in Table 1. The data for $k_{Gas}(660)$ plotted versus $s_{TS}^{1/2}$ have been separated into the pump-forced and wind-forced groups. The figure shows that $k_{Gas}(660)$ is linearly correlated with either $s_{TS}^{1/2}$ and $s_{pH}^{1/2}$, supporting the contention that the convergence rates can be used as proxies for β_{RMS}. Of equal importance however, the data for $k_{Gas}(660)$ plotted versus $s_{TS}^{1/2}$ show that the correlation between the transfer velocity and convergence rate is the same regardless of the forcing mechanism for the near-surface turbulence. This suggests that the convergence rate provides a universal scaling parameter for the transfer velocity.

[35] One important characteristic of the linear relation between $s_{TS}^{1/2}$ or $s_{pH}^{1/2}$ and $k_{Gas}(660)$ is that if s_{TS} or s_{pH} are proxies for β_{RMS}, equation (4) shows that the intercept of the linear relation should be the origin. A least squares regression where the y-intercept was forced through the origin was performed on both data sets. In the case of the regression of $s_{pH}^{1/2}$ and $k_{Gas}(660)$ the coefficient of determination is 0.998 and for the regression of $s_{TS}^{1/2}$ and $k_{Gas}(660)$ it is 0.997. Therefore, the data are consistent with the equation (4). Finally, it should be emphasized that Figure 13 shows that it is possible to correlate k_L with the same fundamental parameter for both wind-generated and mechanically generated turbulence.

5. Conclusions

[36] Using a synthetic jet array tank (SJAT) embedded in a wind tunnel, it was possible to conduct experiments

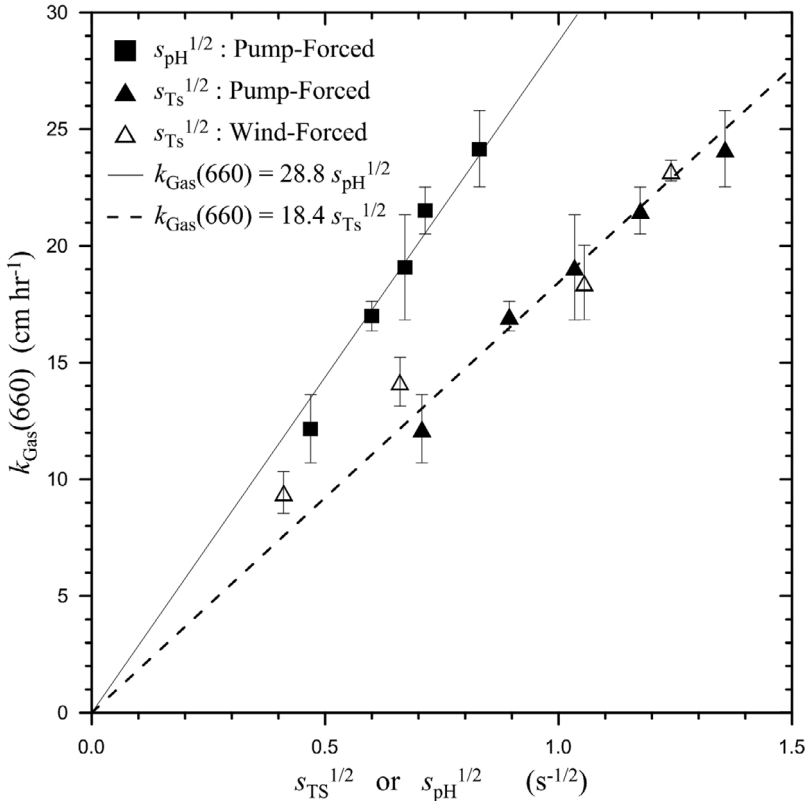

Figure 13. The average transfer velocity of helium and sulfur hexafluoride measured in the SJAT normalized to a Schmidt number of 660, $k_{Gas}(660)$, plotted versus the square root of the convergence rate measured using surface temperature or surface pH, s_{TS} and s_{pH}, respectively. The data key is open triangles, $k_{Gas}(660)$ and s_{TS} measured as a function of wind speed, U, at a constant pump voltage, P_V, of 14 V (i.e., wind-forced); solid triangles, $k_{Gas}(660)$ and s_{TS} measured as a function of pump voltage, P_V, at a constant wind speed, U, of 3.2 m s^{-1} (i.e., pump-forced); solid squares, $k_{Gas}(660)$ and s_{pH} measured as a function of pump voltage, P_V, at a constant wind speed, U, of 3.2 m s^{-1} (i.e., pump-forced). The dashed line shows a least squares regression forced through the origin of the $k_{Gas}(660)$ versus $s_{TS}^{1/2}$ for both the wind-forced and pump-forced data sets. The solid line shows a least squares regression forced through the origin of the $k_{Gas}(660)$ data plotted versus $s_{pH}^{1/2}$ for the pump-forced data. The slopes of the regression lines are shown in the data key.

investigating the air-water transfer of heat and gas in the presence of turbulence generated mechanically below the interface and turbulence generated by shear stress due to the wind. One set of experiments was under conditions where wind speed was kept constant and mechanically generated turbulence was used as the independent variable. A second set of experiments were conducted with mechanically generated turbulence held constant and wind speed made the independent variable. In both cases, the bulk gas transfer velocities of helium and sulfur hexafluoride were measured, IR imagery was used to track water surface temperature fluctuations, and aqueous-phase turbulence was characterized using PIV. In the mechanically forced experiments, surface concentration fluctuations of dissolved CO_2 were measured using a laser-induced fluorescence (LIF) technique.

[37] Increases in either the mechanically generated turbulence intensity or the wind stress were found to be linearly correlated with increases in the bulk gas transfer velocity. Therefore, although the surface boundary layer had different properties for the two forcing mechanisms, the response of the gas flux is consistent in that it increased with the forcing. This supports the conceptual hypothesis that it is the intensity of the aqueous-phase turbulence very near the water surface that controls the exchange of sparingly soluble nonreactive gases.

[38] In the case of transfer driven by mechanically generated turbulence, the LIF surface concentration measurements and water surface temperature imagery showed that the rates at which fluctuations in either pH or temperature occur were correlated with the RMS surface divergence. It is hypothesized that these fluctuations are caused by surface convergence events. Due to continuity, this suggests that measuring either the surface concentration fluctuation rate or the surface temperature fluctuation rate provides a method for scaling the surface divergence relevant for air-water exchange. In support of this, both the temperature and concentration fluctuations rates were found to be linearly related to the surface divergence measured using PIV. Moreover, as predicted by equation (4) it was also shown that the gas transfer velocity was linearly correlated with the square root of the temperature fluctuation rate or the pH fluctuation rate. This suggests that the fluctuation rate measured using IR imagery or surface

fluorescence parameterizes near-surface processes that are fundamental to gas transfer. This implies that as far as the air-water exchange process is concerned, there is no fundamental difference between turbulence generated in the bulk phase that decays upwards toward the air-water interface and turbulence generated at the water surface by the wind stress. Therefore, the possibility remains that there is a method for universally scaling air-water gas exchange at the surface of rivers, lakes, and the ocean.

[39] The results presented above demonstrate that IR imagery provides information that is equivalent to that provided by measuring surface concentration fluctuations and that this information is relevant to air-water gas exchange. In turn, this suggests that developing a method for using IR imagery to measure gas transfer velocities in the field might be possible. However, further work remains to demonstrate conclusively that the surface property fluctuation rates measured here provide a universal scaling mechanism for air-water gas transfer, especially in the presence of larger wind stress and waves.

[40] **Acknowledgments.** This research was supported by the U.S. National Science Foundation under grants OCE-0425305 and OCE-0924992.

References

Asher, W. E., and T. M. Litchendorf (2009), Visualizing near-surface concentration fluctuations using laser-induced fluorescence, *Exp. Fluids*, *46*, 243–253, doi:10.1007/s00348-008-0554-9.

Asher, W. E., and J. F. Pankow (1989), Direct observation of concentration fluctuations close to a gas/liquid interface, *Chem. Eng. Sci.*, *44*, 1451–1455, doi:10.1016/0009-2509(89)85018-3.

Asher, W. E., L. M. Karle, B. J. Higgins, P. J. Farley, E. C. Monahan, and I. S. Leifer (1996), The influence of bubble plumes on air-seawater gas transfer velocities, *J. Geophys. Res.*, *101*, 12,027–12,041.

Asher, W. E., A. T. Jessup, and M. A. Atmane (2004), Oceanic application of the active controlled flux technique for measuring air-sea transfer velocities of heat and gases, *J. Geophys. Res.*, *109*, C08S12, doi:10.1029/2003JC001862.

Atmane, M. A., W. E. Asher, and A. T. Jessup (2004), On the use of the active infrared technique to infer heat and gas transfer velocities at the air-water free surface, *J. Geophys. Res.*, *109*, C08S14, doi:10.1029/2003JC001805.

Banerjee, S., and S. McIntyre (2004), The air-water interface: Turbulence and scalar exchange, in *Advances in Coastal and Ocean Engineering*, edited by J. Grue et al., pp. 181–237, World Sci., Hackensack, N. J., doi:10.1007/978-3-540-36906-6_6.

Banerjee, S., D. Lakehal, and M. Fulgosi (2004), Surface divergence models for scalar exchange between turbulent streams, *Int. J. Multiphase Flow*, *30*, 963–977, doi:10.1016/j.ijmultiphaseflow.2004.05.004.

Brumley, B. H., and G. H. Jirka (1988), Air-water transfer of slightly soluble gases: Turbulence, interfacial processes and conceptual models, *Physicochem. Hydrodyn.*, *10*, 295–319.

Caulliez, G., R. Dupont, and V. I. Shrira (2007), Turbulence generation in the wind-driven subsurface water flow, in *Transport at the Air-Sea Interface: Measurements, Models and Parametrizations*, edited by C. S. Garbe, R. A. Handler, and B. Jähne, pp. 103–117, Springer, Heidelberg, Germany, doi:10.1007/978-3-540-36906-6_7.

Edson, J. B., C. J. Zappa, J. A. Ware, W. R. McGillis, and J. E. Hare (2004), Scalar flux profile relationships over the open ocean, *J. Geophys. Res.*, *109*, C08S09, doi:10.1029/2003JC001960.

Frew, N. M., et al. (2004), Air-sea gas transfer: Its dependence on wind stress, small-scale roughness, and surface films, *J. Geophys. Res.*, *109*, C08S17, doi:10.1029/2003JC002131.

Garbe, C. S., U. Schimpf, and B. Jahne (2004), A surface renewal model to analyze infrared image sequences of the ocean surface for the study of air-sea heat and gas exchange, *J. Geophys. Res.*, *109*, C08S15, doi:10.1029/2003JC001802.

Gui, L., J. Longo, and F. Stern (2001), Biases of PIV measurement of turbulent flow and the masked correlation-based interrogation algorithm, *Exp. Fluids*, *30*, 27–35, doi:10.1007/s003480000131.

Harriott, P. (1962), A random eddy modification of the penetration theory, *Chem. Eng. Sci.*, *17*, 149–154, doi:10.1016/0009-2509(62)80026-8.

Irvine, W. M., and J. B. Pollack (1968), Infrared optical properties of water and ice spheres, *Icarus*, *8*, 324–360, doi:10.1016/0019-1035(68)90083-3.

Janzen, J. G., H. Herlina, G. H. Jirka, H. E. Schulz, and J. S. Gulliver (2010), Estimation of mass transfer velocity based on measured turbulence parameters, *AIChE J.*, *56*(8), 2005–2017.

Jessup, A. T., K. Phadnis, M. A. Atmane, C. J. Zappa, M. R. Loewen, and W. E. Asher (2009), Evidence for complete and partial surface renewal at an air-water interface, *Geophys. Res. Lett.*, *36*, L16601, doi:10.1029/2009GL038986.

Kou, J., and J. R. Saylor (2008), A method for removing surfactants from an air/water interface, *Rev. Sci. Instrum.*, *79*(12), 123907, doi:10.1063/1.3053316.

Magnaudet, J., and I. Calmet (2006), Turbulence mass transfer through a flat shear-free surface, *J. Fluid Mech.*, *553*, 155–185, doi:10.1017/S0022112006008913.

McCready, M. J., E. Vassiliadou, and T. J. Hanratty (1986), Computer simulation of turbulent mass transfer at a mobile interface, *AIChE J.*, *32*, 1108–1115, doi:10.1002/aic.690320707.

McKenna, S. P. (2000), *Free-Surface Turbulence and Air-Water Gas Exchange*, 312 pp., Mass. Inst. of Technol., Cambridge, doi:10.1575/1912/4027.

McKenna, S. P., and W. R. McGillis (2004), The role of free-surface turbulence and surfactants in air-water gas transfer, *Int. J. Heat Mass Transfer*, *47*(3), 539–553, doi:10.1016/j.ijheatmasstransfer.2003.06.001.

Scarano, F., and M. L. Reithmuller (2000), Advances in iterative multigrid PIV image processing, *Exp. Fluids*, *29*, suppl. 1, S051–S060, doi:10.1007/s003480070007.

Schimpf, U., C. S. Garbe, and B. Jahne (2004), Investigation of transport processes across the sea-surface microlayer by infrared imagery, *J. Geophys. Res.*, *109*, C08S13, doi:10.1029/2003JC001803.

Tamburrino, A., and J. S. Gulliver (2002), Free-surface turbulence and mass transfer in a channel flow, *AIChE J.*, *48*, 2732–2743, doi:10.1002/aic.690481204.

Turney, D. E., W. C. Smith, and S. Banerjee (2005), A measure of near-surface fluid motions that predicts air-water gas transfer in a wide range of conditions, *Geophys. Res. Lett.*, *32*, L04607, doi:10.1029/2004GL021671.

Variano, E. A., and E. A. Cowen (2008), A random-jet-stirred turbulence tank, *J. Fluid Mech.*, *604*, 1–32, doi:10.1017/S0022112008000645.

Variano, E., E. Bodenschatz, and E. A. Cowen (2004), A random synthetic jet array driven turbulence tank, *Phys. Fluids*, *37*, 613–615.

Wanninkhof, R., J. R. Ledwell, W. S. Broecker, and M. Hamilton (1987), Gas exchange on Mono Lake and Crowley Lake, California, *J. Geophys. Res.*, *92*, 14,567–14,580.

Westerweel, J., and F. Scarano (2005), Universal outlier detection for PIV data, *Exp. Fluids*, *39*, 1096–1100, doi:10.1007/s00348-005-0016-6.

Willert, C. E., and M. Gharib (1991), Digital particle image velocimetry, *Exp. Fluids*, *10*, 181–193, doi:10.1007/BF00190388.